mater.scichina.com link.springer.com

Published online 6 December 2022 | https://doi.org/10.1007/s40843-022-2259-3
Sci China Mater 2023, 66(4): 1332–1340

Ultrathin thiol-ene crosslinked polymeric electrolyte for solid-state and high-performance lithium metal batteries

Zhifeng Li[1†], Tianyi Wang[1†], Lei Zhong[1*], Min Xiao[1], Dongmei Han[2], Shuanjin Wang[1], Shichao Zhang[3], Sheng Huang[1] and Yuezhong Meng[1*]

ABSTRACT **Solid polymer electrolyte (SPE) is a potential material for the next-generation safe battery system. However, the inability of SPEs to maintain mechanical strength and ionic conductivity is a bottleneck in further research. Here, a poly(ether-thioether) electrolyte with a thiol-ene crosslinked network was prepared by *in situ* click polymerization and supported on an electro-spun polyimide (PI) mat to provide an ultrathin membrane (19 μm in thickness). Combining a thiol-ene crosslinked network and the reinforcement of the electro-spun PI mat, this SPE membrane obtains high storage modulus (135 MPa), high ionic conductivity (2.24×10^{-4} S cm^{-1}), and wide electrochemical window (up to 4.0 V) at 60°C. In addition, the Li-Li symmetrical cell based on the as-prepared electrolyte demonstrates stable cycling performance during Li plating/stripping, lasting more than 800 h at 0.1 mA cm^{-2}. Such $LiFePO_4$/Li cells with an ultrathin thiol-ene network SPE membrane achieve over 250-cycle stability at 0.5 C and 60°C. This work develops a new ultrathin polymer electrolyte for stable solid-state and high-performance lithium metal batteries.**

Keywords: solid polymer electrolyte, electro-spun PI mat, ultrathin, lithium metal battery

INTRODUCTION

Lithium-ion batteries (LIBs) have greatly improved our living standards since their successful commercialization in 1991 [1]. Most commercial LIBs use organic carbonate liquid electrolytes (LEs), which will not only result in the deterioration of battery performance caused by irreversible side reactions between electrolyte and anode, but also cause a series of safety problems, including combustion and explosion [2–5]. Replacing the LE with a solid-state electrolyte (SSE) is an effective way to promote the safety and cycling performance of batteries [6]. In addition, the SSE generally has a higher electrochemical stability window (ESW) than LE; thus, it can match with high-voltage cathode materials and increase the energy density of LIBs [7–9].

SSE can be classified into solid inorganic electrolytes (SIE) and solid polymer electrolytes (SPE) [10]. SIE has been widely researched because of its high ionic conductivity (>10^{-4} S cm^{-1}), excellent thermal stability (>200°C), and nonflammability [11–13]. However, the high cost and poor interface contact between the electrode and electrolyte hinder its development [14]. Compared with SIE, SPE can easily form a compact interface with an electrode. Polyethylene oxide (PEO) is the commonly used SPE because of its ability to complex with lithium ions and chemical stability [15–17]. At present, the application of PEO in the solid-state battery is limited by its low ionic conductivity (10^{-7}–10^{-5} S cm^{-1}) and weak mechanical strength. PEO crystallizes easily at room temperature, while ion transport primarily occurs in the amorphous region of the polymer [18,19]. Therefore, several studies have been conducted to decrease the degree of crystallinity, such as grafting, copolymerization, crosslinking, adding plasticizer, and compositing with inorganic filler [20–28]. Among these methods, copolymerization and crosslinking can effectively decrease crystallinity without losing mechanical strength. Wen *et al.* [29] reported a copolymer with a crosslinked structure, which possessed high ionic conductivity and low interfacial resistance, thus rendering batteries good cycling performance. Zhang *et al.* [30] designed a UV-crosslinked SPE based on PEO. This SPE with a crosslinked network showed great electrochemical performance and successfully suppressed Li dendrite growth. These studies demonstrated an approach to enhance ionic conductivity and mechanical properties from the structural design level.

Furthermore, the thickness of SPE is an important parameter that influences the internal resistance of the battery. Thinner SPE indicates lower impedance and higher energy density for LIBs [12,31,32]. Areal conductance is also a critical parameter for the SPE membrane ($\sigma_s = \sigma/l$, where σ_s, σ, and l represent the conductance per unit area, ionic conductivity, and thickness of SPE, respectively), which is more appropriate to describe ion transport in the battery than ionic conductivity. Therefore, the higher the areal conductance, the better the battery performance [33]. However, fabricating ultrathin SPE is difficult, as its polymer matrix is a soft material that easily cracks. Thus, a thin and robust scaffold material is necessary to obtain ultrathin SPE [34–36]. Wan *et al.* [35] reported an ultrathin composite SPE supported by a vertically aligned porous polyimide (PI) film. The PI film is strong enough to reduce the thickness of SPE to 8.6 μm, and it enables the battery to operate over 1000 h without

[1] The Key Laboratory of Low-carbon Chemistry & Energy Conservation of Guangdong Province/State Key Laboratory of Optoelectronic Materials and Technologies, School of Materials Science and Engineering, Sun Yat-sen University, Guangzhou 510275, China
[2] School of Chemical Engineering and Technology, Sun Yat-Sen University, Zhuhai 519082, China
[3] School of Materials Science and Engineering, Beihang University, Beijing 100083, China
[†] These authors contributed equally to this work.
[*] Corresponding authors: (emails: zhonglei8@mail.sysu.edu.cn (Zhong L); mengyzh@mail.sysu.edu.cn (Meng Y))

short circuit. Recently, Wang *et al.* [34] developed an ultrathin SPE by filling poly(ethylene glycol) methyl ether acrylate and lithium salts into a polyethylene host. Although the ionic conductivity was not so outstanding, the $LiFePO_4$//Li pouch cell assembled with ultrathin SPE could cycle over 1000 times with 76.4% capacity retention. These studies indicate that a strong scaffold material can reduce the thickness of SPE.

In this study, we reported an ultrathin thiol-ene network SPE membrane by *in situ* polymerization, which was reinforced by a PI electro-spun mat. –C–C–O– (EO) and –C–C–S– (ES) chain segments in the thiol-ene network serve as carriers to conduct lithium ions, and the PI electro-spun mat functions as a support matrix to increase the modulus and ensure the continuous phase of the polymer electrolyte matrix, resulting in SPE membrane with a thickness of 19 μm. This ultrathin SPE membrane featured a high storage modulus (135 MPa) and high ionic conductivity (2.24×10^{-4} S cm^{-1}) at 60°C. Consequently, $LiFePO_4$ solid-state batteries based on the as-fabricated SPE membrane demonstrated a high capacity of 146.7 mA h g^{-1} at 0.5 C and 60°C after several activated cycles, and remained at 145.2 mA h g^{-1} after 250 cycles.

EXPERIMENTAL SECTION

Materials

Ethanedithiol (EDT, J&K), diethylene glycol divinyl ether (DGDE, J&K), pentaerythritol *tetra*(3-mercaptopropionate) (PETMP, Sigma), 2,2-dimethoxy-2-phenylacetophenone (DMPA, Aladdin), lithium bis(trifluoromethane sulfonyl)imide (LiTFSI, Macklin), gamma-butyrolactone (GBL, J&K), PEO (M_w: 100,000 g mol^{-1}, Sigma Aldrich), PEO (M_w: 600,000 g mol^{-1}, Sigma Aldrich), $LiFePO_4$ (LFP, Great power Co., Ltd.), Super P (Canrd Co., Ltd.), anhydrous acetonitrile (CH_3CN, J&K), *N*,*N*-dimethylformamide (DMF, J&K), *N*-methyl-2-pyrrolidone (NMP, J&K), chloroform-d ($CDCl_3$, Innochem), PI electro-spun mat (Jiangxi Advanced Nanofiber S&T Co., Ltd.), and lithium foil (Guangzhou Tianlida Chemical Glass Co., Ltd. thickness: 600 μm) were used as received.

Preparation of polymer electrolyte

EDT (3.0 mmol), DGDE (3.2 mmol), PETMP (0.1 mmol), DMPA (0.1 mmol), LiTFSI (1.0 mmol), and GBL (0.1 mL) were added into a glass vial without other solvent and stirred under a dark condition for 0.5 h to obtain a homogeneous precursor solution. The obtained solution was dropped onto a PI electro-spun mat with 10 μm thickness and cured under UV light (365 nm) for 10 min. Afterward, an ultrathin, transparent, and flexible solid membrane (poly(ether-thioether) (PETE)-15/PI10G) was formed (thickness: 19 μm; area density: 2.7 mg cm^{-2}). The experiment was performed in an argon-filled glove box. The PEO electrolyte membrane was prepared as previously reported [37] (thickness: 170 μm; area density: 21.2 mg cm^{-2}). The PEO/PI electrolyte membrane was prepared by solution casting (thickness: 20 μm). The ratio of (EO + ES) or EO to Li for all SPE membranes was 15:1.

Cell assembly and measurements

Homogeneous cathode slurry was obtained by mixing LFP, PEO/LiTFSI, and Super P (*w*/*w*/*w* = 7:2:1) in acetonitrile (ACN)/DMF (*v*/*v* = 1:1) by planetary ball milling at 150 r min^{-1} for 12 h. The slurry was coated with Al foil, followed by drying in an oven at 50°C and further drying at 70°C under a high vacuum for 12 h. LFP was loaded at approximately 1.5 mg cm^{-2}. Before cell assembly, 10 μL of a homogeneous solution (0.05 g mL^{-1}) of PEO and LiTFSI (EO:Li = 15:1) in ACN/DMF was added to the surface of the cathode, followed by drying at room temperature in an argon-filled glove box for 12 h. A 2025-type coin cell was assembled by piling the LFP cathode, SPE, and Li foil together. Charge and discharge tests were conducted to evaluate the cycling performance on a LAND testing system at 60°C in the range of 2.5–3.9 V. A 2032-type Li|SPE|Li symmetric cell was assembled using the same method to evaluate the cycling stability of the SPE and tested at a current density of 0.1 mA cm^{-2} and capacity of 0.1 mA h cm^{-2} at 60°C.

Characterization

The nuclear magnetic resonance (NMR) was recorded on a spectrometer (Bruker, Advance III, 400Hz), using $CDCl_3$ as solvent. Differential scanning calorimeter (DSC) was tested by using a Netzsch Model 204 and heated from −100 to 100°C at a heating rate of 10°C min^{-1} under a nitrogen atmosphere. Thermogravimetric analysis (TGA) was performed from 30 to 700°C at a heating rate of 10°C min^{-1} under nitrogen protection with PerkinElmer Pyris Diamond. Fourier transform infrared spectra (FTIR) were recorded using a spectrometer (PerkinElmer Spectrum 100). Scanning electron microscopy (SEM) was performed by using TESCAN CLARA and JEOL JSM-6380LA. In addition, X-ray photoelectron spectroscopy (XPS) was performed by using Thermo Fisher Scientific ESCA NEXSA. Storage modulus was tested by dynamic mechanical analysis (DMA 242 D) using tensile mode.

Electrochemical measurement

The ionic conductivity was measured by electrochemical impedance spectroscopy (EIS) using NOVE ranging from 1 Hz to 100 kHz. The SPE was sandwiched between two stainless steels (SS), and the ionic conductivity (σ) can be calculated using the following equation:

$$\sigma = \frac{l}{S * R},$$

where l, S, and R represent the thickness, area, and resistance value of the SPE, respectively.

The activation energy can be calculated using the following equation [38,39]:

$$\sigma_i = \sigma_0 \exp\left[-\frac{E_a}{R(T - T_0)}\right],$$

where T_0 is the temperature that is 50 K lower than T_g, T is the Kelvin temperature, E_a is the activation energy, R is the ideal gas constant, and σ_0 is a function of temperature ($\sigma_0 = AT^{-\frac{1}{2}}$), respectively.

The lithium-ion transfer number (t_{Li^+}) was calculated using the Bruce-Vincent-Evans equation [40]:

$$t_{Li^+} = \frac{I_{ss}(\Delta V - I_0 R_0)}{I_0(\Delta V - I_{ss} R_{ss})},$$

where I_0, I_{ss}, R_0, and R_{ss} are the initial current, steady-state current, and interface impendence before and after polarization, respectively. ΔV is the polarization potential (10 mV).

ESW was measured by linear sweep voltammetry (LSV) from 0 to 6 V at 1 mV s^{-1} using a CHI 604E electrochemical work-

station. The SPE was placed between lithium foil and SS or carbon paper.

RESULTS AND DISCUSSION

The design strategy of the PETE-15/PI electrolyte membrane is shown in Fig. 1. Comparing PETE-15/PI with PEO and PEO/PI electrolyte membrane, we solve the common key problems by primarily eliminating the crystal of EO segments by carefully designing a molecular structure, such as, considerably increasing the robustness of electrolyte membranes and decreasing their thickness. PEO is a typical crystalline polymer electrolyte with a low viscous flow temperature. When the PEO electrolyte membrane operates at high temperatures such as 60°C, the polymer chains move faster and even flow, which causes the breaking of the membrane and short circuit of batteries. Using a supported matrix can effectively increase the strength and reduce the thickness of the PEO electrolyte membrane, but the molecular chain can still move out of the supported membrane. Therefore, the broken membrane may block the transmission of Li^+, which degrades battery performance.

Considering the abovementioned problems, we design and fabricate a crosslinked thiol-ene network within a PI electrospun mat to obtain an ultrathin (only 19 μm) and robust electrolyte membrane. The thiol-ene network is superior to other olefin addition networks in conducting Li^+ with the following benefits: (1) the thiol-ene network can conduct ions through main chains, which boosts conductivity; (2) the segment length between crosslinking points can be controlled for an adjustable and uniform network; (3) the alternating structure obtained from thiol-ene addition ingeniously decreases the crystallinity of EO segments. The designed electrolyte membrane exhibits a well-rounded performance, including excellent dimension stability and high ion conductivity.

We investigated the compatibility of the thiol-ene crosslinked network and PI electro-spun mat and the controllable fabrication of the thiol-ene crosslinked network to decouple the trade-off between ionic conductivity and mechanical strength. Fig. 2a shows the chemical structure before and after the polymerization of PETE. The PI electro-spun mat was immersed in a precursor containing EDT, DGDE, PETMP, LiTFSI, and DMPA and then cured under a 365-nm ultraviolet lamp for 10 min. The thiol-ene click addition reaction between thiol and vinyl groups was initiated around PI fibers, which possessed high conversion, rapid rate, and mild reaction conditions (Fig. S1). The composite membrane with 19-μm thickness is light yellow, transparent, integrated, and robust (Fig. 2h, i), demonstrating the excellent compatibility and cooperation between the PI electro-spun mat and PETE. As shown in Fig. S2a, the PI electro-spun mat has a continuous and uniform fiber network and sufficient porosity, which ensures a high content of ionic conductivity in the prepared electrolyte membrane. For the obtained PETE-15/PI membrane, the PI fibers are entirely wrapped in a crosslinked PETE matrix (Fig. S2b). The cross-sectional SEM images of the composite membrane shown in Fig. S2c, d also indicate that the thickness of the composite membrane is 19 μm.

The reaction initiated by the photoinitiator was tracked by ^1H NMR analysis and FTIR spectrum (Fig. 2b, e). The characteristic peaks of EDT and DGDE are approximately 1.7 and 6.5 ppm, corresponding to the hydrogen of sulfhydryl and C=C bond, respectively. In addition, the molar ratio of the thiol group is excessively high. After polymerization, the peak at 6.5 ppm disappears, indicating the complete conversion of double bonds, whereas the peak around 1.7 ppm of ETE is weak, corresponding to the capped thiol group. In the spectrum of ETE, the major peaks can be divided into two parts; the peaks around 2.8 ppm correspond to the hydrogen on the carbon next to the sulfur atom, and the other peaks around 3.6 ppm correspond to the hydrogen on the carbon next to the oxygen atom. The FTIR was selected to characterize the successful preparation of the polymer electrolyte matrix. Fig. 2e shows the FTIR spectra of PETE-15/PI

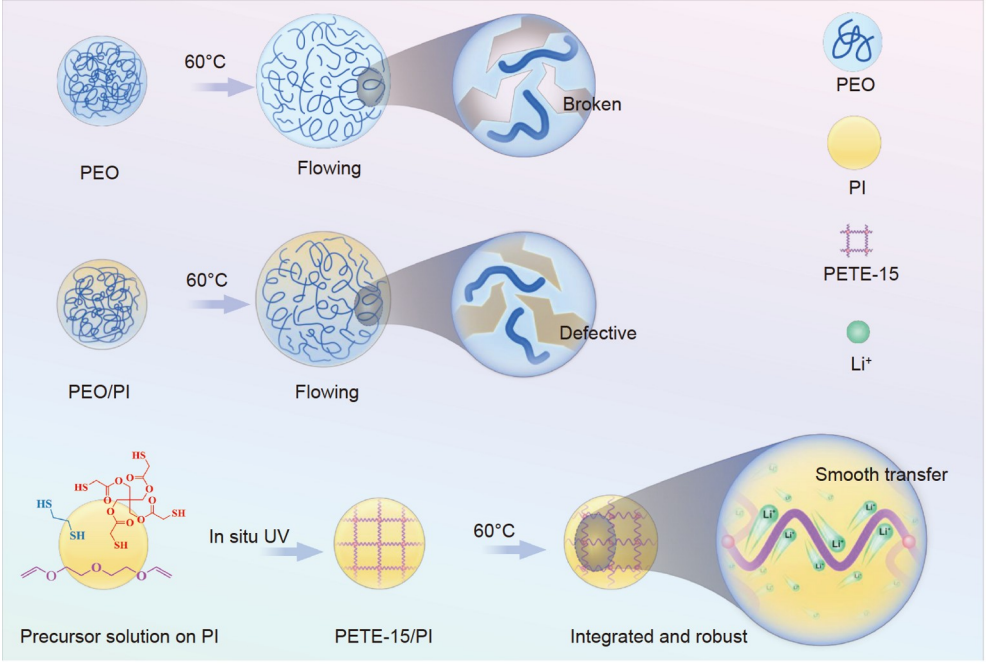

Figure 1 Design of the PETE-15/PI composite electrolyte membrane for improved battery performance. The differences among the PEO electrolyte, PEO/PI electrolyte, and PETE-15/PI electrolyte are displayed.

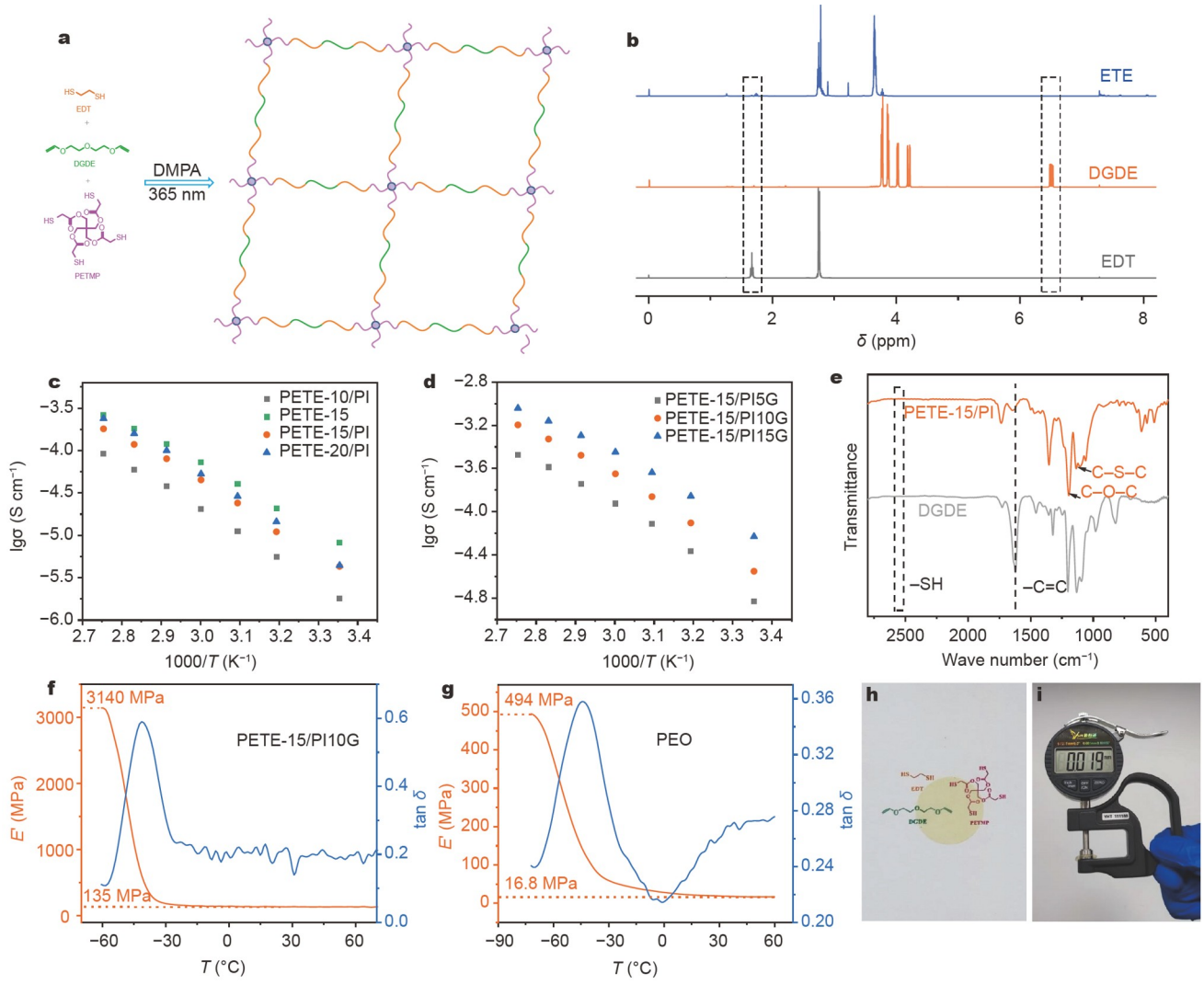

Figure 2 (a) Schematic illustration of the synthesis of PETE-*x via* the thiol-ene click reaction. (b) ^{1}H NMR spectra of EDT, DGDE, and their product of the reaction, ETE. (c) Temperature-dependent ionic conductivities of PETE-*x* with and without PI electro-spun mat. (d) Temperature-dependent ionic conductivities of PETE-15/PI with different ratios of GBL. (e) FTIR spectra of PETE-15/PI and DGDE. Storage modulus of (f) PETE-15/PI10G and (g) PEO electrolyte membrane from −60 to 60°C measured by DMA. (h) Optical image of PETE-15/PI. (i) Thickness of PETE-15/PI.

and DGDE, but EDT and PETMP were not tested because of their strong odor. The absorption peak at 1618 cm^{-1} is ascribed to the C=C stretching vibration of DGDE, which is absent in the spectrum of PETE-15/PI, indicating the complete conversion of DGDE. As reported in the literature, the thiol group in FTIR appears around 2500 cm^{-1}, and no evident peak is observed at this area, implying completely reacted thiol functional groups [41,42]. In addition, the stretching vibrations of C–O–C (1196 cm^{-1}) and C–S–C (1108 cm^{-1}) confirm the chemical structure of PETE-15/PI.

The adjustable thiol-ene network of PETE greatly affects the ionic conductivity and mechanical strength of the PETE-*x*/PI composite membrane. *x* refers to the theoretical structural repeat unit calculated by the ratio of reactants. The thiol-ene click reaction is in accordance with the rule of the step-growth reaction mechanism accompanied by the chain transfer reaction of sulfur-free radicals. *x* follows the equation $x = r/(1 - r)$, where *r* is the mole ratio of EDT/DGDE. We matched up *r* and *x*. When we select a higher *r* approaching 1, *x* is larger, which indicates a thiol-ene network with a lower crosslinking density. Therefore, we further explored the relationship between the chain length *x* and ionic conductivity. As shown in Fig. 2c, the ionic conductivity is improved, when *x* increases from 10 to 20, which can be attributed to the enhancement of the segmental motion as the crosslinking degree declines. We also selected PETE-15 as a preferential option to fabricate the PETE-15/PI composite membrane for an overall consideration of conductivity and mechanical strength. Fig. 2c shows the ionic conductivity of PETE-15 with and without a PI electro-spun mat, and the results indicate that the addition of PI electro-spun fiber slightly decreases the ionic conductivity. To enhance ionic conductivity, 5, 10, and 15 wt.% GBL was added in PETE-15/PI, labeled PETE-15/PI5G, PETE-15/PI10G, and PETE-15/PI15G, respectively. The temperature-dependent ionic conductivities of these three electrolytes are shown in Fig. 2d. With high conductivities of 2.80 × 10^{-5} S cm^{-1} at 25°C and 2.24 × 10^{-4} S cm^{-1} at 60°C, PETE-15/PI10G was applied for the assembly and performance test of subsequent batteries. Furthermore, we applied the Vogel-Tamman-Fulcher (VTF) equation to describe the relationship between the conductivity and temperature for

the PETE-15/PI10G and PEO electrolyte membrane (Fig. S3). The lower activation energy (E_a) calculated for PETE-15/PI10G indicates fast ion transportation through the thiol-ene network. Another outstanding merit of the alternating thiol-ene structure lies in the high lithium-ion transfer number (t_{Li^+}) of PETE-15/PI10G. Fig. 3c exhibits its interfacial resistance before and after polarization and polarization current curve. t_{Li^+} of the PETE-15/PI10G electrolyte membrane is calculated to be 0.31, whereas that of the PEO electrolyte membrane is only 0.11 (Fig. S4c). Higher t_{Li^+} promotes the weakened coordination of EO segments and lithium ions in PETE-15/PI10G, which indicates the success of designing the alternating structure of ES segments and EO segments.

In previous reports, the mechanical property of SPE is usually characterized by tensile tests at room temperature. However, it cannot reveal the actual strength at high temperatures during battery tests. Therefore, we utilized DMA to analyze the storage modulus of the electrolyte membrane at different temperatures. As shown in Fig. 2f, the storage modulus of the PETE-15/PI10G electrolyte membrane achieves 3140 MPa at −60°C and remains 135 MPa at 60°C, which is superior to the PEO electrolyte membrane (Fig. 2g). The PETE-15/PI10G electrolyte membrane has an interpenetrating network of thiol-ene crosslinked network and PI electro-spun fiber network. Therefore, it maintains a high storage modulus of more than 135 MPa at 60°C, whereas the PEO electrolyte membrane loses its modulus dramatically from 494 to 16.8 MPa at −60 to 60°C.

For a polymer electrolyte, a lower glass transition temperature (T_g) indicates more free volume, which can promote segmental motion and increase ionic conductivity. As shown in Fig. 3a, PETE-15/PI10G shows T_g of −45.5°C, without any melting peak, which confirms its amorphous structure. This finding can be attributed to the introduction of ES segments in the polymer chain. By contrast, higher T_g and melting peaks are observed in the DSC curve of the PEO electrolyte (Fig. S4a). In addition, T_g of PETE-*x*/PI decreases with the increase of *x* and the amount of GBL (Fig. S5), which is consistent with the ionic conductivity variation rules. Furthermore, TGA was conducted to evaluate the thermal stability of the polymer electrolytes. Fig. 3b shows the TGA curve of PETE-15/PI10G. 5 and 50 wt% weight loss can be obtained at 144 and 319°C, respectively, which can meet the requirement of thermal stability in LIBs. The derivative thermogravimetry (DTG) curve shows three evident peaks corresponding to the decomposition of GBL, polymer matrix, and lithium salt. Two thermal decomposition temperatures (321 and 451°C) belong to PETE and LiTFSI, respectively, which can also be verified in the TGA curve of the PETE-15/PI electrolyte (Fig. S6a). In addition, the thermal decomposition temperature of the PI support matrix is over 500°C (Fig. S6b).

LSV was applied to evaluate the electrochemical stability of the polymer electrolyte at 60°C. As shown in Fig. S7, when taking SS as the counter electrode, the response current rapidly increases at 4.8 V, indicating the electrochemical oxidation decomposition of the PETE-15/PI10G electrolyte membrane. However, using SS as the working electrode cannot accurately test LSV as reported in previous literature because SS is smooth, flat, and inert, whereas the cathode is porous and rough [43,44]. Therefore, we used carbon paper as the counter electrode to test the electro-

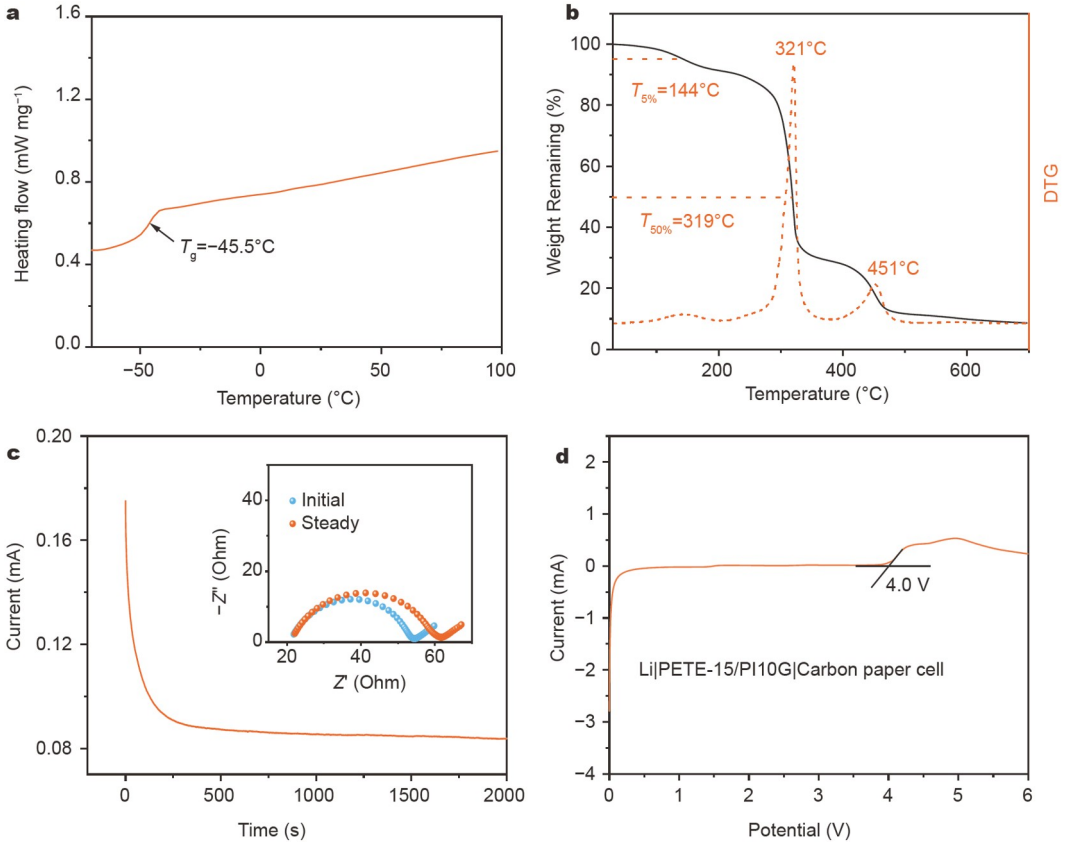

Figure 3 (a) DSC curve; (b) TGA and DTG curves of PETE-15/PI10G. (c) Chronoamperometry curve of Li|PETE-15/PI10G|Li cell at 60°C (inset: EIS spectra before and after polarization); (d) LSV of Li|PETE-15/PI10G|carbon paper cell at 60°C.

chemical stability, and the result suggests that the ESW of the PETE-15/PI10G electrolyte membrane is 4.0 V (Fig. 3d), which can meet the application requirement of LIBs.

To investigate the lithium/electrolyte interface stability, the lithium plating/stripping cycling experiment was performed at 60°C. We designed a test procedure, including charge and discharge processes for 1 h, at a current density of 0.1 mA cm^{-2}. Fig. 4a shows the time-voltage curves of the lithium symmetric cell with PETE-15/PI10G and PEO electrolyte membranes. The Li|PETE-15/PI10G|Li cell presents a low overpotential of 44 mV at the early cycle and increases slightly until 800 h. Meanwhile, no short circuit occurs during lithium plating/stripping, indicating its good mechanical strength and compatibility with lithium metal. Moreover, the Li|PETE-15/PI|Li cell exhibits a stable overpotential and no short circuit over 1400 h (Fig. S8). By contrast, the Li|PEO|Li cell presents an overpotential of 77 mV at the first cycle and reaches a stable state of 42 mV after several activation cycles. However, the symmetric cell shows micro short circuit at 172 h and short circuit at 207 h (Fig. 4c), which is primarily due to poor dimensional stability. We also prepared a PEO/PI electrolyte membrane using solution casting and tested the symmetric cell at the same condition. The cell shows short circuit at 40 h, which indicates the superiority of the PETE-15/PI10G electrolyte (Fig. S9). Fig. S10 illustrates the difference in dimensional stability between PETE-15/PI10G and PEO electrolyte membranes. We raised the temperature to 70°C to observe the result more quickly, whereas the melting point of the PEO electrolyte is 49.8°C (Fig. S4a). After thermal insulation for 24 h, the PETE-15/PI10G electrolyte membrane can keep its shape, but the PEO electrolyte membrane has observable deformation. This property will make it easier for cell failure, particularly in coin cells with high-stress structures.

As for liquid lithium metal batteries, the side reaction between LE and lithium anode is an important problem, which will cause an unstable solid electrolyte interface layer and uneven lithium plating. As shown in Fig. 4f, ununiform lithium plating is observed at the surface after 200 h of continuous testing in Li|LE|Li cells. By contrast, the surface of the cycled Li|PETE-15/PI10G|Li cell is dense and smooth (Fig. 4e), which is almost the same as that of the cell before cycling (Fig. S11). The result indicates a stable interface between PETE-15/PI10G and lithium anode. For further explaining the lithium/polymer electrolyte interfaces, XPS analysis was selected to illustrate the composition information of the Li surface after cycling. As shown in Fig. S12,

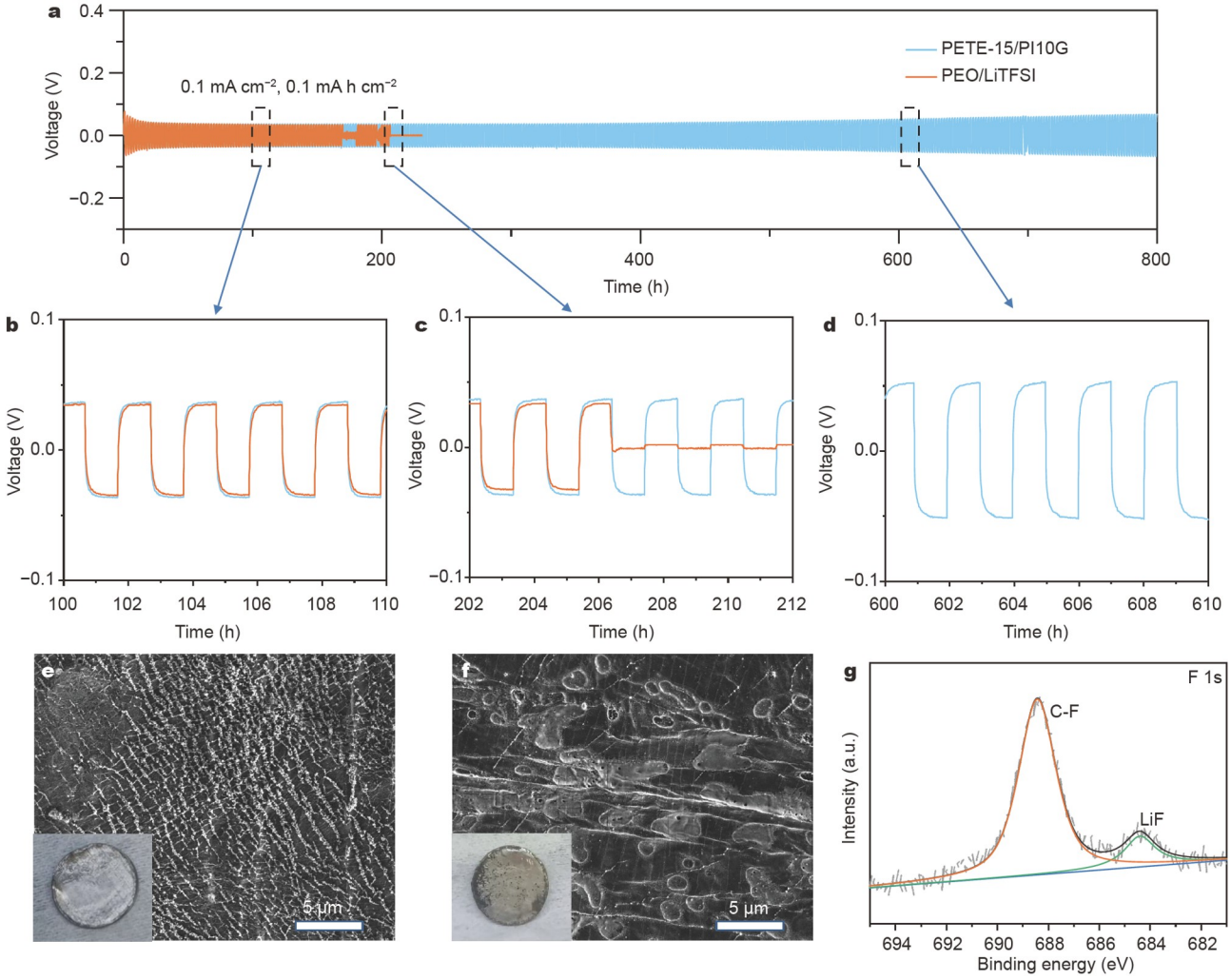

Figure 4 (a) Galvanostatic cycling performances of Li|PETE-15/PI10G|Li and Li|PEO|Li cells at 0.1 mA cm^{-2}, 60°C. Voltage-time profiles of Li|PETE-15/PI10G|Li cells from (b) 100–110 h, (c) 202–212 h, and (d) 600–610 h. Surface SEM images of the lithium foil disassembled from (e) Li|PETE-15/PI10G|Li and (f) Li|LE|Li after 200 h of cycling. (g) XPS spectrum of F 1s for the lithium foil disassembled from Li|PETE-15/PI10G|Li after 200 h of cycling.

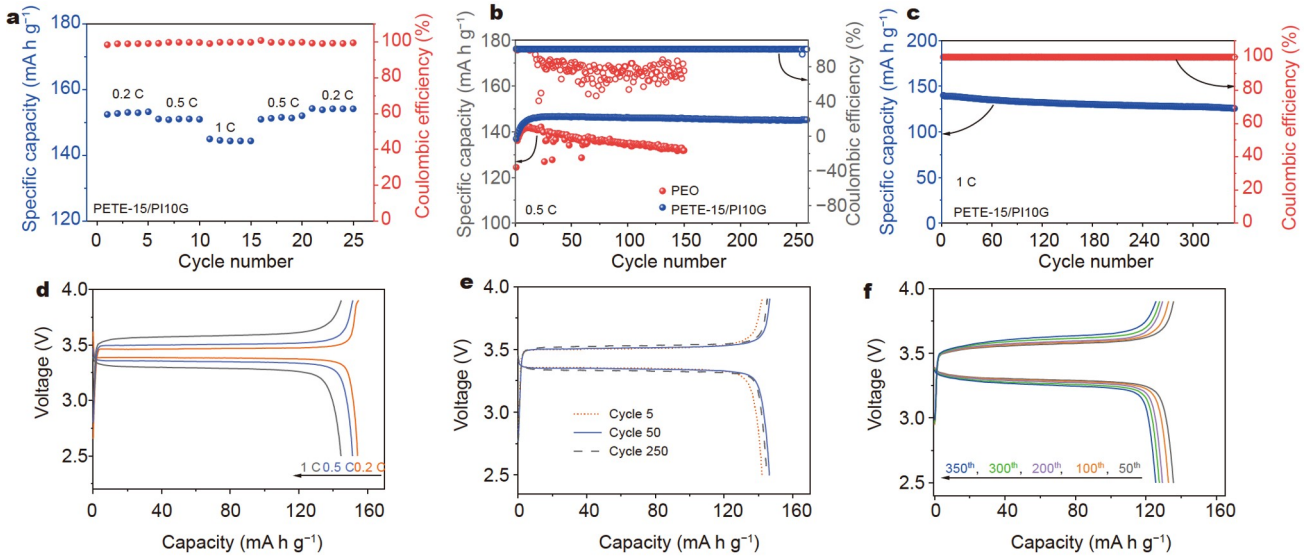

Figure 5 (a) Rate performance of the Li|PETE-15/PI10G|LFP cells. (b) Long-term cycling performance of the Li|PETE-15/PI10G|LFP and Li|PEO|LFP cells at 0.5 C. (c) Long-term cycling performance of the Li|PETE-15/PI10G|LFP cells at 1 C. (d) Voltage-capacity profile of the Li|PETE-15/PI10G|LFP cells at different charge rates. Voltage-capacity profiles of the Li|PETE-15/PI10G|LFP cells at (e) 0.5 C and (f) 1 C. The experiments were conducted at 60°C.

three peaks in the C 1s spectra are attributed to C–C, C–O, and C=O [45,46], which are primarily derived from reactions between the polymer electrolyte and Li anode during Li plating and striping. As previously reported, LiF is a useful component of solid electrolyte interface, which can achieve uniform Li electrodeposition [47]. In the F 1s spectrum (Fig. 4g), the peaks of C–F and LiF are derived from lithium salt.

Finally, we explored the potential application of PETE-15/PI10G in lithium batteries. The 2025-type coin cells were assembled using Li metal as the anode, PETE-15/PI10G as the SPE, and LFP as the cathode material. As shown in Fig. S13, two peaks are observed at 3.70 and 3.18 V, which correspond to the de-intercalation and intercalation of Li-ion. The Li|PETE-15/PI10G|LFP cell shows satisfactory reversibility of electrochemical reaction because of the similar area of oxidation and reduction peak. The rate performance of the Li|PETE-15/PI10G|LFP cell is shown in Fig. 5a. The cell delivers a high capacity of 153.3 mA h g^{-1} at 0.2 C with the Coulombic efficiency of 99.2%. At a higher current density, the discharge capacity can reach 151.1 and 144.4 mA h g^{-1} at 0.5 and 1 C, respectively, with the Coulombic efficiency of 99.9%. In addition, the capacity of 154.2 mA h g^{-1} can be maintained in the last five cycles, indicating its outstanding rate performance. Fig. 5d shows the voltage-capacity curves at different rates. The cell has low overpotentials of 56, 81, and 156 mV at 0.2, 0.5, and 1 C, respectively, which can be attributed to the thickness of the polymer electrolyte. Fig. 5b represents the cycling stability of the Li|PETE-15/PI10G|LFP cell at 60°C. At 0.5 C rate, the specific capacity can achieve 146.7 mA h g^{-1} after several activated cycles and remain at 145.2 mA h g^{-1} after 250 cycles (average Coulombic efficiency: 99.9%), which is 99.0% of the highest capacity. By contrast, the Li|PEO|LFP cell provides the specific capacity of 142.1 mA h g^{-1} and decays to 130.1 mA h g^{-1} rapidly with worse Coulombic efficiency from cycle 21 (Fig. S4d). Moreover, the Li|PEO/PI|LFP cell can cycle 16 times and fail (Fig. S14). This excellent cycling performance is primarily due to the compatibility of the PETE-15/PI10G electrolyte membrane with Li anode and its dimensional stability and high storage modulus. Even at a higher discharge rate (1 C), the Li|PETE-15/PI10G|LFP cell can also deliver 139.9 mA h g^{-1} at the initial cycle and remain 124.8 mA h g^{-1} after 360 cycles (retention rate: 89.2%, Fig. 5c). Furthermore, the loss capacity is due to the worsening of battery polarization (Fig. 5f). These results indicate that the PETE-15/PI10G electrolyte exhibits an enormous potential for the practical application of LIBs.

CONCLUSIONS

An ultrathin PETE-15/PI10G electrolyte membrane was successfully designed and fabricated *via* a thiol-ene click reaction within a PI electro-spun mat. Compared with the conventional PEO electrolyte membrane, the PETE-15/PI10G electrolyte membrane exhibits the storage modulus up to 135 MPa and ionic conductivity of 2.24 × 10^{-4} S cm^{-1} at 60°C. These outstanding performances can be attributed to the construction of an adjustable and uniform network containing EO and ES chain segments on the PI electro-spun mat. Such LFP/Li cells with the ultrathin PETE-15/PI10G electrolyte membrane exhibit an excellent rate performance (144.4 mA h g^{-1} at 1 C) and cycling stability (99.0% retention rate after 250 cycles at 0.5 C). This work provides a simple, rapid, and high-efficiency approach for an ultrathin SPE membrane in lithium batteries.

Received 16 June 2022; accepted 15 September 2022; published online 6 December 2022

1 Zhou Q, Ma J, Dong S, *et al.* Intermolecular chemistry in solid polymer electrolytes for high-energy-density lithium batteries. Adv Mater, 2019, 31: 1902029
2 Cui Y, Wan J, Ye Y, *et al.* A fireproof, lightweight, polymer-polymer solid-state electrolyte for safe lithium batteries. Nano Lett, 2020, 20: 1686–1692
3 Zhou B, Yang M, Zuo C, *et al.* Flexible, self-healing, and fire-resistant polymer electrolytes fabricated *via* photopolymerization for all-solid-state lithium metal batteries. ACS Macro Lett, 2020, 9: 525–532
4 Song Y, Liu X, Ren D, *et al.* Simultaneously blocking chemical crosstalk and internal short circuit *via* gel-stretching derived nanoporous non-

shrinkage separator for safe lithium-ion batteries. Adv Mater, 2022, 34: 2106335
5 Vishnugopi BS, Kazyak E, Lewis JA, *et al.* Challenges and opportunities for fast charging of solid-state lithium metal batteries. ACS Energy Lett, 2021, 6: 3734–3749
6 Xi G, Xiao M, Wang S, *et al.* Polymer-based solid electrolytes: Material selection, design, and application. Adv Funct Mater, 2021, 31: 2007598
7 Tan DHS, Banerjee A, Chen Z, *et al.* From nanoscale interface characterization to sustainable energy storage using all-solid-state batteries. Nat Nanotechnol, 2020, 15: 170–180
8 Liu H, Cheng XB, Huang JQ, *et al.* Controlling dendrite growth in solid-state electrolytes. ACS Energy Lett, 2020, 5: 833–843
9 Cui G, Tominaga Y. Polymer electrolytes toward next-generation batteries. Macro Chem Phys, 2022, 223: 2200013
10 Zhao Q, Stalin S, Zhao CZ, *et al.* Designing solid-state electrolytes for safe, energy-dense batteries. Nat Rev Mater, 2020, 5: 229–252
11 Famprikis T, Canepa P, Dawson JA, *et al.* Fundamentals of inorganic solid-state electrolytes for batteries. Nat Mater, 2019, 18: 1278–1291
12 Balaish M, Gonzalez-Rosillo JC, Kim KJ, *et al.* Processing thin but robust electrolytes for solid-state batteries. Nat Energy, 2021, 6: 227–239
13 Fan L, Wei S, Li S, *et al.* Recent progress of the solid-state electrolytes for high-energy metal-based batteries. Adv Energy Mater, 2018, 8: 1702657
14 Li S, Zhang S, Shen L, *et al.* Progress and perspective of ceramic/polymer composite solid electrolytes for lithium batteries. Adv Sci, 2020, 7: 1903088
15 Xue Z, He D, Xie X. Poly(ethylene oxide)-based electrolytes for lithium-ion batteries. J Mater Chem A, 2015, 3: 19218–19253
16 Xiao Y, Wang Y, Bo SH, *et al.* Understanding interface stability in solid-state batteries. Nat Rev Mater, 2019, 5: 105–126
17 Cheng J, Hou G, Sun Q, *et al.* A novel coral-like garnet for high-performance PEO-based all solid-state batteries. Sci China Mater, 2022, 65: 364–372
18 Sarapas JM, Tew GN. Poly(ether-thioethers) by thiol-ene click and their oxidized analogues as lithium polymer electrolytes. Macromolecules, 2016, 49: 1154–1162
19 Yue L, Ma J, Zhang J, *et al.* All solid-state polymer electrolytes for high-performance lithium ion batteries. Energy Storage Mater, 2016, 5: 139–164
20 Zhong L, Wang S, Xiao M, *et al.* Addressing interface elimination: Boosting comprehensive performance of all-solid-state Li-S battery. Energy Storage Mater, 2021, 41: 563–570
21 Lv Z, Zhou Q, Zhang S, *et al.* Cyano-reinforced *in-situ* polymer electrolyte enabling long-life cycling for high-voltage lithium metal batteries. Energy Storage Mater, 2021, 37: 215–223
22 Xu R, Xiao B, Xuan C, *et al.* Facile and powerful *in situ* polymerization strategy for sulfur-based all-solid polymer electrolytes in lithium batteries. ACS Appl Mater Interfaces, 2021, 13: 34274–34281
23 Liu Y, Zhao Y, Lu W, *et al.* PEO based polymer in plastic crystal electrolytes for room temperature high-voltage lithium metal batteries. Nano Energy, 2021, 88: 106205
24 Fan LZ, He H, Nan CW. Tailoring inorganic-polymer composites for the mass production of solid-state batteries. Nat Rev Mater, 2021, 6: 1003–1019
25 Zhang B, Zhang Y, Zhang N, *et al.* Synthesis and interface stability of polystyrene-poly(ethylene glycol)-polystyrene triblock copolymer as solid-state electrolyte for lithium-metal batteries. J Power Sources, 2019, 428: 93–104
26 Meabe L, Huynh TV, Mantione D, *et al.* UV-cross-linked poly(ethylene oxide carbonate) as free standing solid polymer electrolyte for lithium batteries. Electrochim Acta, 2019, 302: 414–421
27 Zhou B, Jiang J, Zhang F, *et al.* Crosslinked poly(ethylene oxide)-based membrane electrolyte consisting of polyhedral oligomeric silsesquioxane nanocages for all-solid-state lithium ion batteries. J Power Sources, 2020, 449: 227541
28 Wang Q, Dong T, Zhou Q, *et al.* An *in-situ* generated composite solid-state electrolyte towards high-voltage lithium metal batteries. Sci China Chem, 2022, 65: 934–942
29 Wen P, Zhao Y, Wang Z, *et al.* Solvent-free synthesis of the polymer electrolyte *via* photo-controlled radical polymerization: Toward ultra-fast in-built fabrication of solid-state batteries under visible light. ACS Appl Mater Interfaces, 2021, 13: 8426–8434
30 Zhang Y, Lu W, Cong L, *et al.* Cross-linking network based on poly (ethylene oxide): Solid polymer electrolyte for room temperature lithium battery. J Power Sources, 2019, 420: 63–72
31 He F, Tang W, Zhang X, *et al.* High energy density solid state lithium metal batteries enabled by sub-5 μm solid polymer electrolytes. Adv Mater, 2021, 33: 2105329
32 Wu J, Rao Z, Cheng Z, *et al.* Ultrathin, flexible polymer electrolyte for cost-effective fabrication of all-solid-state lithium metal batteries. Adv Energy Mater, 2019, 9: 1902767
33 Wu J, Yuan L, Zhang W, *et al.* Reducing the thickness of solid-state electrolyte membranes for high-energy lithium batteries. Energy Environ Sci, 2021, 14: 12–36
34 Wang Z, Shen L, Deng S, *et al.* 10 μm-thick high-strength solid polymer electrolytes with excellent interface compatibility for flexible all-solid-state lithium-metal batteries. Adv Mater, 2021, 33: 2100353
35 Wan J, Xie J, Kong X, *et al.* Ultrathin, flexible, solid polymer composite electrolyte enabled with aligned nanoporous host for lithium batteries. Nat Nanotechnol, 2019, 14: 705–711
36 Xu Y, Zhang S, Liang T, *et al.* Porous polyamide skeleton-reinforced solid-state electrolyte: Enhanced flexibility, safety, and electrochemical performance. ACS Appl Mater Interfaces, 2021, 13: 11018–11025
37 Lu J, Zhou J, Chen R, *et al.* 4.2 V poly(ethylene oxide)-based all-solid-state lithium batteries with superior cycle and safety performance. Energy Storage Mater, 2020, 32: 191–198
38 Mindemark J, Lacey MJ, Bowden T, *et al.* Beyond PEO—Alternative host materials for Li^+-conducting solid polymer electrolytes. Prog Polym Sci, 2018, 81: 114–143
39 Wang H, Sheng L, Yasin G, *et al.* Reviewing the current status and development of polymer electrolytes for solid-state lithium batteries. Energy Storage Mater, 2020, 33: 188–215
40 Evans J, Vincent CA, Bruce PG. Electrochemical measurement of transference numbers in polymer electrolytes. Polymer, 1987, 28: 2324–2328
41 Xuan C, Gao S, Wang Y, *et al. In-situ* generation of high performance thiol-conjugated solid polymer electrolytes *via* reliable thiol-acrylate click chemistry. J Power Sources, 2020, 456: 228024
42 Wang H, Wang Q, Cao X, *et al.* Thiol-branched solid polymer electrolyte featuring high strength, toughness, and lithium ionic conductivity for lithium-metal batteries. Adv Mater, 2020, 32: 2001259
43 Homann G, Stolz L, Nair J, *et al.* Poly(ethylene oxide)-based electrolyte for solid-state-lithium-batteries with high voltage positive electrodes: Evaluating the role of electrolyte oxidation in rapid cell failure. Sci Rep, 2020, 10: 4390
44 Yang X, Jiang M, Gao X, *et al.* Determining the limiting factor of the electrochemical stability window for PEO-based solid polymer electrolytes: Main chain or terminal –OH group? Energy Environ Sci, 2020, 13: 1318–1325
45 Deng K, Guan T, Liang F, *et al.* Flame-retardant single-ion conducting polymer electrolytes based on anion acceptors for high-safety lithium metal batteries. J Mater Chem A, 2021, 9: 7692–7702
46 Deng K, Zhou S, Xu Z, *et al.* A high ion-conducting, self-healing and nonflammable polymer electrolyte with dynamic imine bonds for dendrite-free lithium metal batteries. Chem Eng J, 2022, 428: 131224
47 Lu Y, Tu Z, Archer LA. Stable lithium electrodeposition in liquid and nanoporous solid electrolytes. Nat Mater, 2014, 13: 961–969

Acknowledgements This work was supported by the National Key Research and Development Program (2019YFA0705701), the National Natural Science Foundation of China (22179149, 22075329, 22008267, 51573215 and 21978332), the Basic and Applied Basic Research Foundation of Guangdong province (2021A0505030022, 2019A1515010803 and 2020A1515011445), and Guangzhou Scientific and Technological Planning Project (201804020025 and 201904010271).

Author contributions Li Z and Wang T carried out the project and wrote the original draft; Zhong L and Meng Y refined the draft and supervised the project; Xiao M, Han D, Wang S, Zhang S, and Huang S contributed to the data analysis and discussion. All authors contributed to the general discussion.

Conflict of interest The authors declare that they have no conflict of interest.

Supplementary information Supporting data are available in the online version of the paper.

Zhifeng Li is currently a ME candidate at the School of Material Science and Engineering, Sun Yat-sen University. He received his BE degree from Sun Yat-sen University in 2020. His research interest is solid polymer electrolytes and their applications in LIBs.

Tianyi Wang received his BE degree from the School of Materials Science and Engineering, Sun Yat-sen University in 2016. He is studying for a doctorate degree under the supervision of Prof. Yuezhong Meng at Sun Yat-sen University.

Lei Zhong received her PhD degree from the School of Material Science and Engineering, Sun Yat-sen University in 2018. She became a postdoctoral and associate research fellow at the School of Materials Science and Engineering, Sun Yat-sen university in 2018 and 2020, respectively. Her research interest includes solid electrolytes and their applications in energy devices, such as lithium sulfur batteries.

Yuezhong Meng received his BSc, MSc, and PhD degrees from Dalian University of Technology. He worked at the City University of Hong Kong, McGill University, Nanyang Technological University and the National University of Singapore for more than 8 years. He became a "Hundred Talents" member of Chinese Academy of Sciences in 1998. Now he is a Pearl-River professor at Sun Yat-sen University and the director of the Key Laboratory of Low-carbon Chemistry and Energy Conservation of Guangdong Province.

超薄烯-巯交联聚合物电解质及其固态高性能锂金属电池

李志峰[1†], 王天羿[1†], 钟雷[1*], 肖敏[1], 韩东梅[2], 王拴紧[1], 张世超[3], 黄盛[1], 孟跃中[1*]

摘要 固态聚合物电解质(SPE)是下一代安全电池系统的潜在材料, 但SPE不能同时保持较高的机械强度和离子传导率, 使下一步研究进入瓶颈. 在此, 我们通过原位点击反应在静电纺丝聚酰亚胺(PI)膜上制备了一种具有交联结构的聚醚硫醚电解质, 厚度仅为19 μm. 由于烯-巯网络的交联结构和静电纺丝PI膜的增强作用, 该SPE膜在60°C下具有135 MPa的储能模量, 2.24 × 10^{-4} S cm^{-1}的离子传导率和4.0 V的电化学稳定窗口, 并且锂-锂对称电池在0.1 mA cm^{-2}下循环超过800 h, 展现出了优异的循环稳定性. 用该超薄聚合物电解质膜组装的$LiFePO_4$/Li电池在60°C, 0.5 C下能够循环超过250圈. 这项工作开发了一种用于固态高性能锂金属电池的新型聚合物电解质.